FULL PAPER

Li-Ion Batteries

ADVANCED
MATERIALS
INTERFACES

www.advmatinterfaces.de

Elucidating the Mechanism Involved in the Performance Improvement of Lithium-Ion Transition Metal Oxide Battery by Conducting Polymer

Taehoon Kim, Luis K. Ono, and Yabing Qi*

Surface treatments with conducting polymers are effective in ameliorating charge capacities and cycling performances for a wide range of lithium-ion batteries such as Li-layered transition metal oxide, Li-sulfur, and Li-air batteries. So far, however, very little is known about the key process directly involved with the improvement of cell performance and stability. The present study examines how a conducting polymer can contribute to charge capacity enhancement, employing poly(3,4-ethylenedioxythiophene):poly(styrene-sulfonate) coating on the lithium-layered transition metal oxide cathode. The property of the electrode interface layer is studied on the basis of the local atomic environments. The conducting polymer not only hinders the formation of LiF, carbonates, and semicarbonates compounds but also renders the nature of the solid-electrolyte interphase layer formed during electrochemical cycles. Furthermore, it inhibits the dissolution of the active material into the electrolyte and preserves the initial atomic states including the active material bulk. The coating enables good consistency in the local atomic environment with depth at the electrode interface, which in turn impedes the phase mismatch resulting from the surface reconstruction on the layered oxide electrode. This further mitigates the phase transformation of the active material, resulting in a lower voltage decay on charge–discharge.

1. Introduction

Li-ion batteries (LiBs) have been extensively used as power sources in a wide range of applications owing to their high energy densities, suitable rate capabilities, low self-discharge properties, and a range of working voltages accessible with flexible designs.[1–6] The successful commercialization of the Li-ion batteries has led to the development of the next-generation electrode materials for high power electric vehicles and aerospace applications.[7–10]

Dr. T. Kim, Dr. L. K. Ono, Prof. Y. B. Qi
Energy Materials and Surface Sciences Unit (EMSSU)
Okinawa Institute of Science and Technology Graduate University (OIST)
1919-1 Tancha, Onna-son, Okinawa 904-0495, Japan
E-mail: Yabing.Qi@OIST.jp

The ORCID identification number(s) for the author(s) of this article can be found under https://doi.org/10.1002/admi.201801785.

Thackeray et al. proposed the Li-rich transition metal oxide cathode, represented as $x\text{Li}_2\text{MnO}_3 \cdot (1-x)\text{LiMO}_2$ (M = Mn, Co, Ni), to achieve extra capacity ($\approx$250 mAhg^{-1}) from the compound of $\text{Li}[\text{Li}_{1/3}\text{Mn}_{2/3}]\text{O}_2$ at high voltage (>4.5 V).[11,12] Since then, a number of Li-rich layered oxide derivatives have been developed. In recent years, researchers have shown a considerable interest in Ni-rich layered oxide batteries such as $\text{Li}(\text{Ni}_{0.8}\text{Co}_{0.1}\text{Mn}_{0.1})\text{O}_2$, $\text{Li}(\text{Ni}_{0.5}\text{Co}_{0.2}\text{Mn}_{0.3})\text{O}_2$, and $\text{Li}(\text{Ni}_{0.6}\text{Co}_{0.2}\text{Mn}_{0.2})\text{O}_2$ due to their high discharge capacity (>220 mAhg^{-1}) and good compatibility with diverse electrolytes.[13,14] Whereas the conversion type of electrode materials (e.g., LiS, LiSe, and Li-Air) has drawn some attention most recently, the transition metal oxide intercalation materials (NMC) are still the major type of electrodes for the rechargeable batteries commercially available at present.[15] Much effort has been devoted to the improvement of the electrochemical performance of the batteries. However, the capacity fading and voltage decay attributed to the irreversible modification in the atomic states of the transition metals still remain to be solved. Designing a stable electrochemistry cell involves the adjustment of the battery stability window to the chemical potentials of the anode and cathode, which are likely to be determined by the energy of the redox couples of individual transition metal ions. It is the redox energy level relative to the O:2p band and the formal oxidation state (valence state) of the metal cations (3d states) in the electronic structure that impose the intrinsic limitation on the cell voltage of the transition metal oxide batteries.[6,16–18] Hence, maintaining the initial electronic structure of the electrode material is crucial as it is designed to efficiently transport the electrons during Li$^+$ (de)intercalation within a particular voltage range. Numerous studies, however, have found that the electronic structure undergoes irreversible modifications upon charge–discharge.[19–24] The change in the electronic structure, that is, modifications in the energy versus electronic density of states driven by collective changes in the redox couple of transition metals and anions can further evolve into the transformation of the electrode structure. Previous studies have reported the crystallography transformation from a layered structure into a spinel structure during subsequent cycles in a Li-rich transition metal oxide cathode.[25–27] The structural transformations triggered by atomic state changes become more complex because of the variations in the local atomic and crystallographic

environments between the electrode surface and bulk. Whereas the layered structure ($R\bar{3}m$) is the majority in the bulk electrode, the spinel ($Fd\bar{3}m$) and rock salt structures ($Fm\bar{3}m$) can emerge on the surface as a consequence of the surface reconstruction via the transition metal migration and the oxygen evolution in the layered oxide cathodes.[14,28–31] It is well known that the surface reconstruction impedes Li-ion diffusion and accelerates transition metals dissolution into the electrolyte, thus leading to irreversible capacity loss of the battery.[28,31,32] The reconstructed surface is also strongly associated with the redox reactions with the electrolyte. An example of this reaction is the dissolution of Mn^{2+} originated from the disproportional reaction of $2Mn^{3+} \rightarrow Mn^{2+} + Mn^{4+}$ by acidic attack (e.g., HF) in the spinel electrode.[33–36] The redox reactions are generally coupled with the formation of surface layers composed of undesired byproducts such as LiF, Li_2CO_3, and alkyl carbonates (($ROCO_2Li)_2$ or $ROCO_2Li$). The solid-electrolyte interphase (SEI) layer consisting of multiple organic and inorganic components grows during charge and discharge.[33,36,37] An unstable SEI layer formed at the electrode not only reduces the ionic and the electron conductivities but also triggers some redox reactions with electrolytes, leading to further SEI formation, voltage decay, and capacity fading.[6,35,36] Collectively, the aforementioned reactions are likely to generate a series of phase mismatches between the electrode bulk, surface, and interface. Surface treatments with conducting polymers such as polyaniline (PANi), polypyrrole (PPy), polydopamine (PDA), and poly-3,4-ethylenedixoythiophene (PEDOT) have been proven to be effective in improving the electrochemical performance and stability of lithium-ion batteries (e.g., NMC, Li-rich NMC, silicon-based LiB, LiS, and Li-Air), hindering the unstable SEI formation.[38–50] In particular, PEDOT has drawn much attention due to its superior conductivity, thermal stability, and mechanical flexibility.[51–53] The rate capability of $LiFePO_4$ cell could be improved by developing a freestanding PEDOT-$LiFePO_4$ composite as the battery active material.[54] $LiNi_{1/3}Co_{1/3}Mn_{1/3}O_2$ cathode revealed an enhanced capacity and thermal stability after a PEDOT coating on the active material.[55] Manganese oxide nanowires for lithium-ion battery anodes also benefit from the poly(3,4-ethylenedioxythiophene):polystyrene sulfonate (PEDOT:PSS) coating, as it leads to better electrochemical activities, mitigating the active material pulverization.[50] A previous study also explored the improvement in the cycling stability and discharge capacity of Li-rich transition metal oxide batteries (e.g., $Li_{1.2}Ni_{0.2}Mn_{0.6}O_2$) by the surface modification with PEDOT:PSS.[56] Another study revealed the enhanced cycling and thermal stabilities of a Ni-rich cathode, that is, $LiNi_{0.6}Co_{0.2}Mn_{0.2}O_2$ (NCM622) by a double-layer coating with PEDOT and Al_2O_3.[39] It is not only the transition metal oxide batteries but also the lithium-sulfur and the lithium-air batteries that profit from the conducting polymer treatments.[46,47,49,57] Extensive research has demonstrated the notable effects of the conducting polymers on the electrochemical properties and the material stabilities. So far, however, very little is known about the fundamental understanding of the process and nature involved in the significant improvements of the applications.

Herein, by employing PEDOT:PSS on $LiNi_{1/3}Co_{1/3}Mn_{1/3}O_2$ active material, we present a surface interface study that holds the key to the mechanism involved in assisting the improvement of electrode performance and stability for lithium-ion batteries.

In the current study, the surface treatment with PEDOT:PSS not only improves the electrochemical performance but also leads to the formation of a stable SEI layer with a uniform distribution of the interface components. In addition, the treatment effectively impedes the further formation of the Li_2CO_3 and LiF during electrochemical cycles, thereby providing a better diffusion environment for Li^+. As a protective layer, the polymer can also preserve the active material from the dissolution into the electrolyte or the HF attack. The present study, for the first time, elucidates that the process involved with the improvement of the electrochemical performance by the conducting polymer is attributed to the distinct mitigation of the atomic phase mismatches between the cathode interface, surface, and bulk.

2. Results and Discussion

Secondary ion mass spectrometry (SIMS) depth profiling is a well-established method to characterize the SEI formation at the cycled electrode materials. In the current study, the depth profiles of some positive ions were successfully visualized based on the positive ion detection (PID) mode of SIMS (**Figure 1**). Particular attention is paid to the distribution of Li^+ at the cathode as a function of depth. Interestingly, the PEDOT:PSS coated $Li(Ni_{1/3}Mn_{1/3}Co_{1/3})O_2$ cathode (labeled as PEDOT) revealed a homogenous distribution of Li^+ after consecutive electrochemical cycles. By contrast, the bare $Li(Ni_{1/3}Mn_{1/3}Co_{1/3})O_2$ cathode (labeled as NMC) showed a concentration gradient of Li^+ after subsequent charge–discharge as can be seen in Figure 1b. This discrepancy could be explained by the formation of dissimilar SEI layers. The SEI layer at the PEDOT cell is likely to be more stable and thinner than that of the NMC cell, allowing a better environment for Li^+ conduction. On the other side, the SEI layer formed at the NMC cathode appears to be instable and complex because of the by-products originated from the reactions between Li^+ and the electrolyte (or salt). The formation of Li_2O, Li_2CO_3, LiF, and carbonate materials (e.g., $(ROCO_2Li)_2$ and $ROCO_2Li$) at the interface could hinder Li^+ from uniform migration into the cathode. The key components detected in the SEI layer will be discussed in a later part with X-ray photoelectron spectroscopy (XPS) analyses. Also, there was a distinct difference in the distribution of the carbon element between the cycled PEDOT and the cycled NMC cathode. Whereas the cycled NMC cell showed a blurry carbon band with nonuniform distribution with depth (Figure 1b), the cycled PEDOT cell exhibited a clearer and narrower carbon band with a homogeneous distribution with depth as shown in Figure 1a. The formation into a carbon band which contains ^{12}C can be explained by the presence of the different carbon types from the conductive additive (carbon black, Super C65) and the carbonate SEI components, that is, Li_2CO_3, $(ROCO_2Li)_2$, and $ROCO_2Li$. It is therefore likely that a wider carbon band indicates a higher number of carbonate species at the electrode interface, which deteriorates the ionic conductivity of Li^+. A more detailed discussion on the results with positive ion detection is given in the last part of the current section. **Figure 2**a,b compares the galvanostatic profile between the PEDOT:PSS coated $Li(Ni_{1/3}Mn_{1/3}Co_{1/3})O_2$ cell and the bare $Li(Ni_{1/3}Mn_{1/3}Co_{1/3})O_2$ cell in the voltage window of 2.0–4.2 V at room temperature. The cell with the PEDOT:PSS coating has shown significantly higher charge and discharge capacity
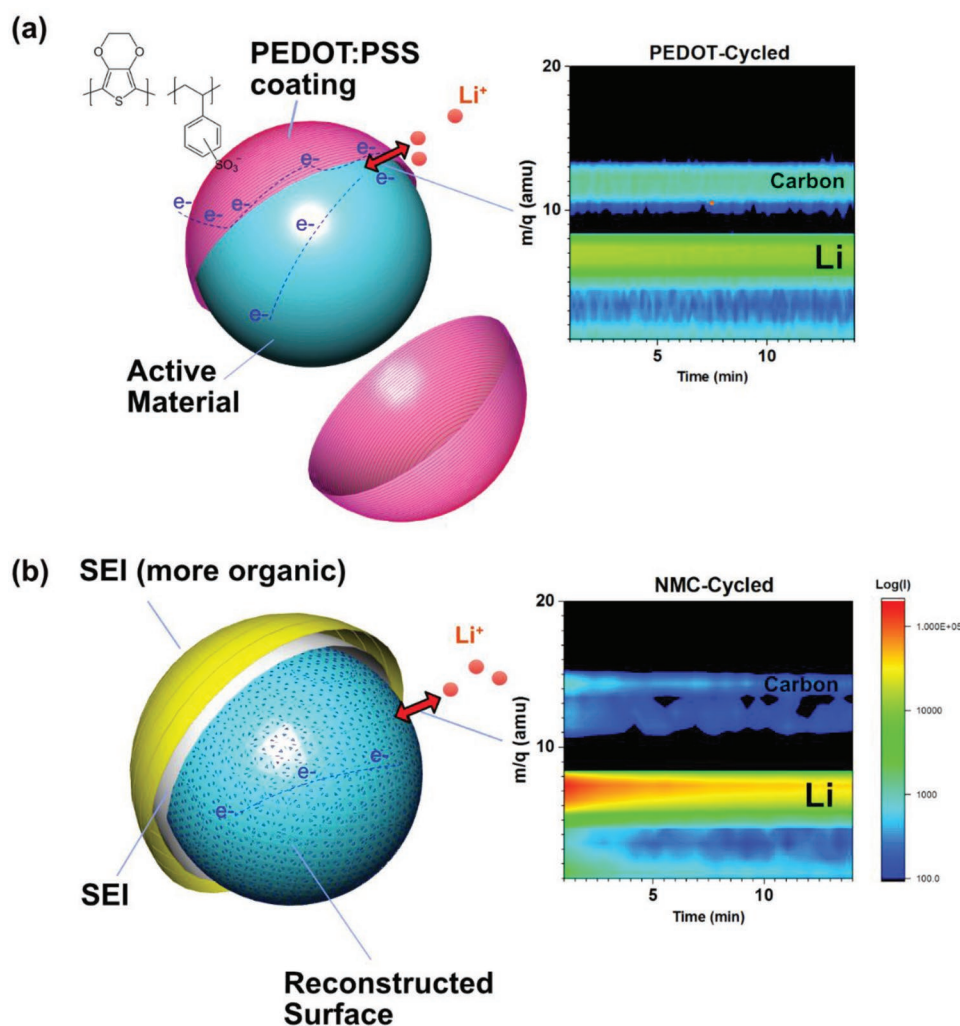
Figure 1. Schematics of surface condition of active material particles with corresponding SIMS positive ion detection (PID) measurements under Ar-gas environment. a) Surface interface of PEDOT:PSS coated Li(Ni$_{1/3}$Mn$_{1/3}$Co$_{1/3}$)O$_2$ cathode cycled between C and 3C rate (labeled as PEDOT). b) Surface interface of Li(Ni$_{1/3}$Mn$_{1/3}$Co$_{1/3}$)O$_2$ cathode (NMC) cycled between C and 3C rate (labeled as NMC). Y-axis represents the atomic mass of positive ions ($1 \leq m \leq 20$) including isotopes. Time is the Ar-sputtering time, which can be related to the depth of SEI layer.

especially at fast charge rates and better retention performance during electrochemical cycles (Figure 2c). The improved cell performance can be explained by the enhanced electron conductivity, as the coated polymer material offers high electrical conductivity (≈300 S cm^{-1}) due to the clear phase separation between the deprotonated sulfonyl group with negative charge and the poly(3,4-ethylenedioxythiophene) part with positive charge. In addition, the coating layer seemed to be effective in suppressing some side reactions between the electrode and electrolyte during electrochemical cycles, as evidenced by the dQ/dV plot. Another important observation is the voltage shifts of the reduction peaks at around 3.70–3.72 V at the fifth cycle. Whereas the shift of the reduction peak toward lower voltages (3.70 to ≈3.40 V) was remarkable for the bare NMC cell, the voltage shift was very small (3.72–3.71 V) for the PEDOT:PSS coated cell upon charge–discharge (Figure 2d,e). The intensity change in this peak is likely to be caused by the charge compensation mechanism by the two-stage oxidation change of Ni^{2+}/Ni^{3+}/Ni^{4+}, but the spectral shift to a lower voltage is probably associated with the Mn phase transition associated with the crystal transformation from a layered structure into a spinel structure. Also, the voltage decay was relatively smaller in the cell with the PEDOT:PSS treatment as shown in Figure 2a,b. An evaluation of the voltage stability window of the PEDOT:PSS coated electrode has been provided (Figure S4, Supporting Information). The surface morphology of the bare NMC cathode and the cathode with PEDOT:PSS coating is compared in Figure 2f. The active material particles in the cycled Li(Ni$_{1/3}$Mn$_{1/3}$Co$_{1/3}$)O$_2$ cell were segregated from the electrode matrix. Some of those particles appeared to be severely disrupted. By contrast, there was no isolation of the active material particles in the cycled cathode with the PEDOT:PSS coating. The initial coating condition was well maintained after electrochemical cycles. Electrochemical impedance spectroscopy (EIS) was chosen to assess the resistances of the SEI layer (R_{SEI}) and the charge transfer (R_{CT}) between the electrolyte and electrode after cycling (Table S4, Supporting Information). In addition, Li$^+$ diffusivity was evaluated from the Warburg impedance of the Nyquist plot (Figure 2g). Both at pristine state
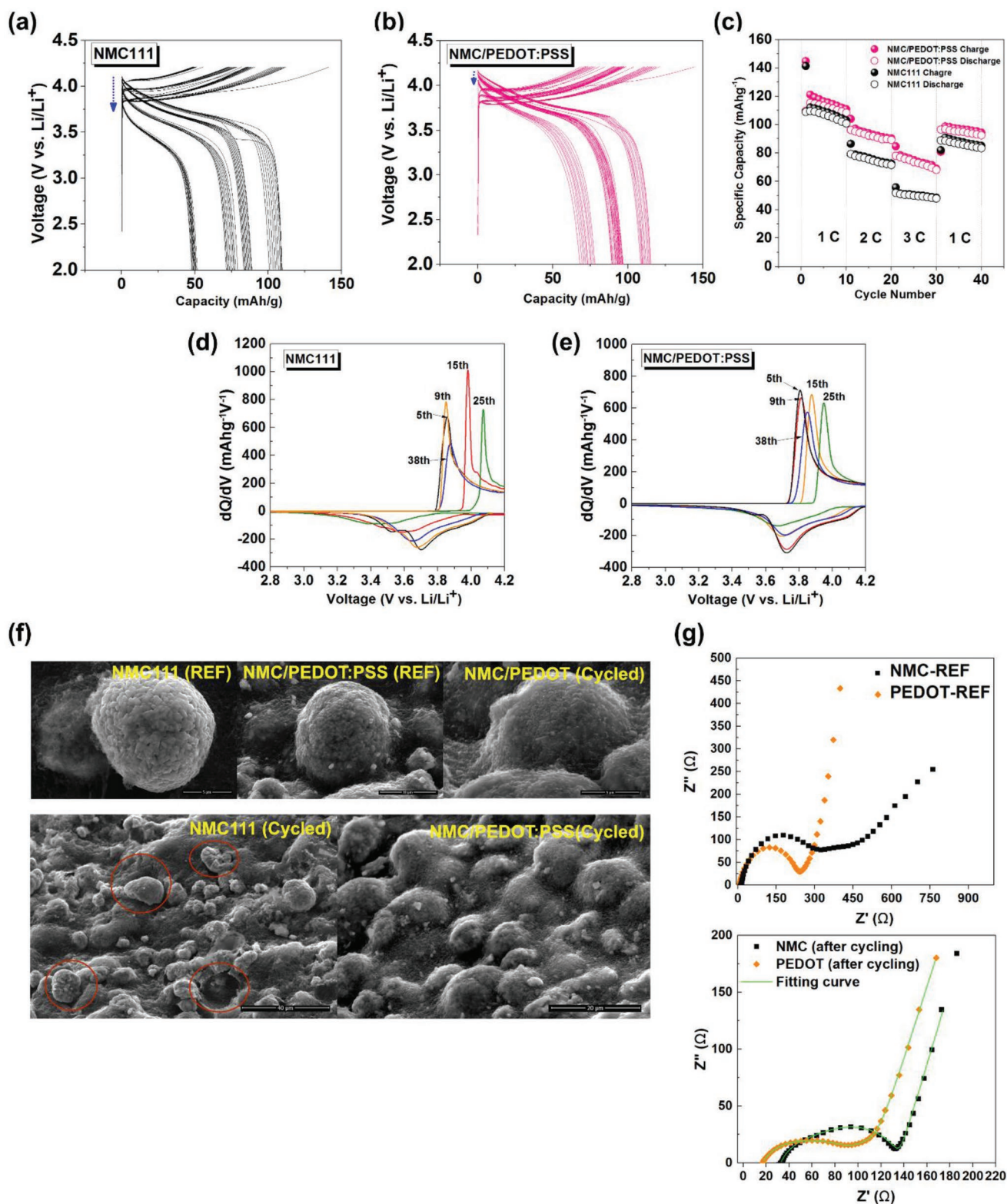
Figure 2. a,b) Galvanostatic profile of PEDOT:PSS coated Li(Ni$_{1/3}$Mn$_{1/3}$Co$_{1/3}$)O$_2$ cathode (PEDOT) and bare Li(Ni$_{1/3}$Mn$_{1/3}$Co$_{1/3}$)O$_2$ cathode (NMC) cycled in the voltage window of 2.0–4.2 V. The blue arrow indicates the voltage decay on charge–discharge. c) Rate capability between the corresponded cathodes cycled from C to 2C to 3C, and back to C-rate. d,e) dQ/dV plots of PEDOT:PSS coated Li(Ni$_{1/3}$Mn$_{1/3}$Co$_{1/3}$)O$_2$ cell and bare Li(Ni$_{1/3}$Mn$_{1/3}$Co$_{1/3}$)O$_2$ cell. f) SEM images of the corresponding cathodes before and after cycling. g) Nyquist plots of NMC and PEDOT cells at pristine state (REF) and after cycling (cycled from C to 2C to 3C and back to C-rate).
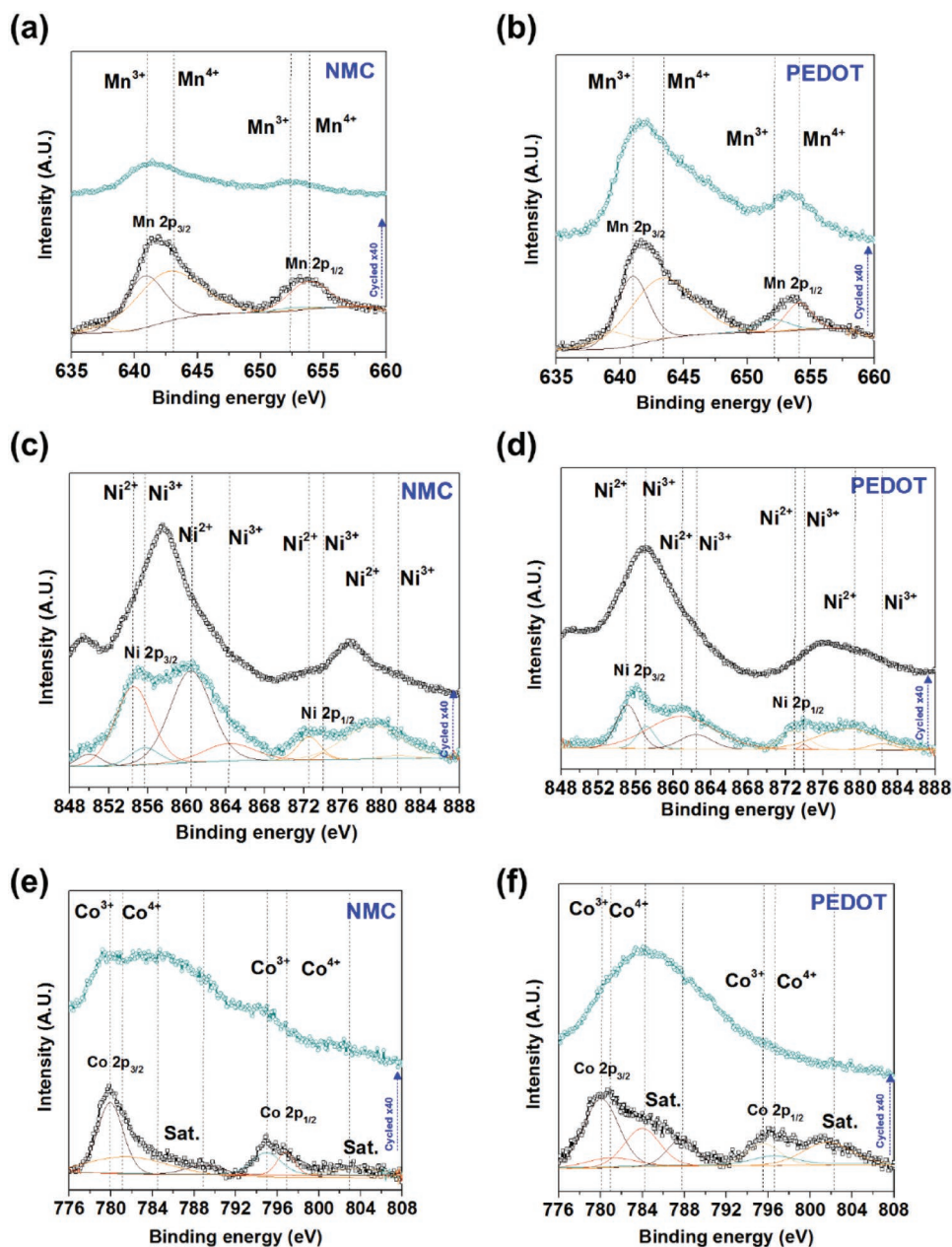
ADVANCED
Science NEWS
www.advancedsciencenews.com

ADVANCED
MATERIALS
INTERFACES
www.advmatinterfaces.de

Figure 3. a,b) XPS spectra of transition metals. Mn 2p of the cycled bare $Li(Ni_{1/3}Mn_{1/3}Co_{1/3})O_2$ (labeled as NMC) and PEDOT:PSS coated $Li(Ni_{1/3}Mn_{1/3}Co_{1/3})O_2$ cathode (labeled as PEDOT). c,d) Ni 2p of the cycled NMC cathode and PEDOT cathode. e,f) Co 2p of the cycled NMC cathode and PEDOT cathode. Sat. indicates satellite peak.

(REF) and cycled state, PEDOT:PSS coated $Li(Ni_{1/3}Mn_{1/3}Co_{1/3})O_2$ cell revealed lower resistances, as shown in Figure 2g. At cycled state, the resistance from the electrolyte (R_{el}) was measured to be 32.75 and 16.5 Ω for NMC and PEDOT cell (Table S4, Supporting Information), respectively. PEDOT cell is less likely than NMC cell to suffer from the active material dissolution by the electrolyte. Also, the SEI impedance of PEDOT cell (31.14 Ω) was lower than that of the NMC cell (40 Ω). The charge transfer impedance (R_{CT}) was 62 Ω for NMC cell and 37.3 Ω for PEDOT cell, suggesting lower interfacial resistance of the PEDOT:PSS coated electrode during the charge compensation process. The PEDOT cell revealed higher Li^+ diffusivity (9.18725×10^{-11} cm^2 s^{-1}) than

the NMC cell (6.42264×10^{-11} cm^2 s^{-1}), and this finding is in good agreement with the visualized SIMS measurements at the electrode/electrolyte interphase. It appears that the conducting polymer not only protects the active material but also improves the electrochemical reaction kinetics.

A surface-chemistry study was conducted by XPS to gain insight into the property of the SEI layer formed after charge and discharge. **Figure 3** compares the XPS spectra of the transition metals (Mn 2p, Ni 2p, and Co 2p) between the bare $Li(Ni_{1/3}Mn_{1/3}Co_{1/3})O_2$ cell (denoted as NMC) and the PEDOT:PSS coated $Li(Ni_{1/3}Mn_{1/3}Co_{1/3})O_2$ cell (denoted as PEDOT). The binding energies of Mn ($2p_{3/2}$) and Mn ($2p_{1/2}$)

**ADVANCED
SCIENCE NEWS**
www.advancedsciencenews.com

**ADVANCED
MATERIALS
INTERFACES**
www.advmatinterfaces.de

were ≈642.0 and 653.9 eV, respectively, at the pristine state for the NMC cathode, indicating the presence of Mn^{4+}.[58] The binding energy was 641.9 for Mn $(2p_{3/2})$ and 653.9 eV for Mn $(2p_{1/2})$ at the pristine state for the PEDOT cathode. No significant difference was detected in the Mn 2p spectra at the pristine state between both cathodes. However, there was a distinct difference in the peak location and intensity of Mn 2p between the NMC and PEDOT cathode after the electrochemical cycles. Whereas the NMC cathode revealed a dramatic intensity decrease in the Mn 2p peak and a spectral shift toward a lower binding energy (Figure 3a), the PEDOT cathode exhibited little change in the Mn 2p spectra suggesting effective protections against side reactions from the electrolyte (Figure 3b). The oxidation state of the Mn tends to remain tetravalent at the surface of PEDOT cathode upon charge–discharge. The Ni $(2p_{3/2})$ and Ni $(2p_{1/2})$ peaks were observed at 854.9 and 872.5 eV followed by the shake-up peaks identified at around 860.5 and 879.1 eV, respectively, indicating the presence of Ni^{2+} in the NMC pristine state (Figure 3c,d). Two minor peaks assigned to the Ni^{3+} were also found at 855.7 and 874.0 eV. The appearance of these minor peaks can be explained by the electron transfer between Mn^{4+} and Ni^{2+}. On the other hand, there was a marked spectral change of Ni^{2+} (854.9 and 872.5 eV) to higher binding energies (≈857 and ≈876.7 eV) after the NMC cell cycling. The Ni $(2p_{3/2})$ and Ni $(2p_{1/2})$ peaks were found at 854.9 and 872.9 eV followed by the shake-up peaks observed at around 860.8 and 879.0 eV for the PEDOT cathode. The location of the Ni 2p peaks for the PEDOT cathode is almost identical to that of the NMC cathode at the pristine state. After cycling, the spectra of Ni^{2+} slightly shifted from 854.9 to 856.9 eV for the PEDOT cell (Figure 3d). This shift is apparently smaller as compared with NMC cell, suggesting less modification in the local atomic environment of Ni in the PEDOT cathode. Ni is known to be a key contributor to the charge compensation mechanism by its two-stage oxidation changes between Ni^{2+}/Ni^{3+} and Ni^{3+}/Ni^{4+} upon charge–discharge. It is not only the energy shift but also the notable intensity drop in the shoulder of the Ni peak (at around 861 and 881 eV) that could be observed in the uncoated cathode after cycling. The $Li(Ni_{1/3}Mn_{1/3}Co_{1/3})O_2$ coated with PEDOT:PSS is less likely than the NMC cathode to undergo the atomic state changes in Ni. Figure 3e,f shows the XPS spectra obtained from the Co 2p of the NMC and PEDOT cathode. The Co $(2p_{3/2})$ and Co $(2p_{1/2})$ peaks were shown at 779.9 and 794.7 eV, respectively, for the NMC cathode. The satellite peaks were also observed at around 789.0 and 802.7 eV. The XPS peaks of Co 2p were found at 780.6 eV for Co $(2p_{3/2})$ and 759.9 eV for Co $(2p_{1/2})$ of the PEDOT cathode. There were satellite peaks at ≈789.0 and 802.7 eV. Some weak peaks were also identified at 781.0 and 796.0 eV for the NMC cathode and at 780.9 and 796.5 eV for the PEDOT cathode. These peaks are the indication of Co^{3+}, and thus suggest the coexistence of Co^{3+} and Co^{4+} in the pristine state on both cathodes. On the other side, there was a notable difference between the NMC and PEDOT cathode after the electrochemical cycles. While both cathodes underwent spectral shifts, the NMC cathode slightly shifted to a lower binding energy followed by accumulation of some by-products, possibly resulting from the interaction between the electrode and the electrolyte during charge and discharge. It has been studied that a Co element reduced to a lower

oxidation state (e.g., Co^{2+}) with high spin configuration at the electrode surface is essentially connected to the formation of the SEI layer, and the involvement of the reduced Co has been observed particularly at the voltage window of 4.0–4.3 V.[18] Taken together, the findings deduced from the surface chemistry suggest that the polymer coating plays an important role in preventing the transition metal dissolution from the acidic attack by HF. The decomposition of the salt ($LiPF_6 \rightarrow PF_5 + LiF$) in the electrolyte is known to be the dominant process of the formation of HF ($PF_5 + H_2O \rightarrow PF_3O + 2HF$), which in turn dissolves the Mn through Hunter's disproportionation mechanism.[59–61] Also, the conducting polymer tends to maintain the initial atomic states of the transition metal elements after charge and discharge. The maintenance of the surface state by PEODT:PSS during electrochemical cycles was also evaluated by ultraviolet photoelectron spectroscopy (UPS) measurements, as presented in Figures S2 and S3 (Supporting Information). The NMC cathode underwent a significant work function change after cycling, as compared with the PEDOT cathode (Figure S3, Supporting Information). On the other hand, the PEDOT cathode appears to be more metallic than the NMC cathode both at reference and cycled states (Figure S2, Supporting Information). The XPS analyses on O 1s, C 1s, and F 1s are compared in **Figure 4**. These are the key elements that are strongly associated with the formation of SEI layer. XPS measurements of O1s are shown in Figure 4a,b. The peak at around 529.1 eV is attributed to the oxygen ions in the crystal lattice indicating the presence of the transition metal oxides.[18,62] The peak at ≈531.5 eV can be assigned to the existence of Li_2CO_3 and/or metal carbonates, which are the major inorganic species in the SEI layer.[33,37,62,63] The spectrum of O 1s in the NMC cathode is comparable to that of PEDOT cathode, but the intensity of the peak was slightly lower than that for the PEDOT sample. The PEDOT:PSS coating that covers the active material may cause a signal decrease of the lattice oxygen. After electrochemical cycles, there was a significant difference in the XPS O 1s spectra between the NMC and PEDOT cathode. Whereas the NMC cathode showed a dramatic increase of the Li_2CO_3 component (Figure 4a), the change was minimum for the PEDOT cathode (Figure 4b). The C 1s spectra with three major peaks at 283.9, 285.3, and 290.0 eV are shown in Figure 4c,d. The large peak at 283.9 eV is related to the conductive carbon.[64,65] On the other hand, those peaks at 285.3 eV (C−H) and 290.0 eV (C−F) are likely to be associated with the polyvinylidene fluoride (PVDF) binder.[37,66] During charge–discharge, no important change was observed in the conductive carbon peak. However, there was a difference in the intensity of the C−H peak between the two cathodes. It appears that the PVDF binder of the NMC cathode tends to degrade faster than that of the PEDOT cathode.[67] Spectra collected from F 1s are presented in Figure 4e,f. A large peak was found at 687.2 eV at the pristine state for both samples. After cycling, the intensity reduction of this peak was notably higher for the NMC cathode as compared with the PEDOT cathode. The result is in good agreement with the C 1s measurements, as it suggests the faster degradation of the PVDF binder in the NMC cathode. It should also be noted that the curve fitting to the F 1s spectra of the cycled NMC cathode differed from that of the cycled PEDOT cathode. The occurrence of the LiF peak (685 eV for
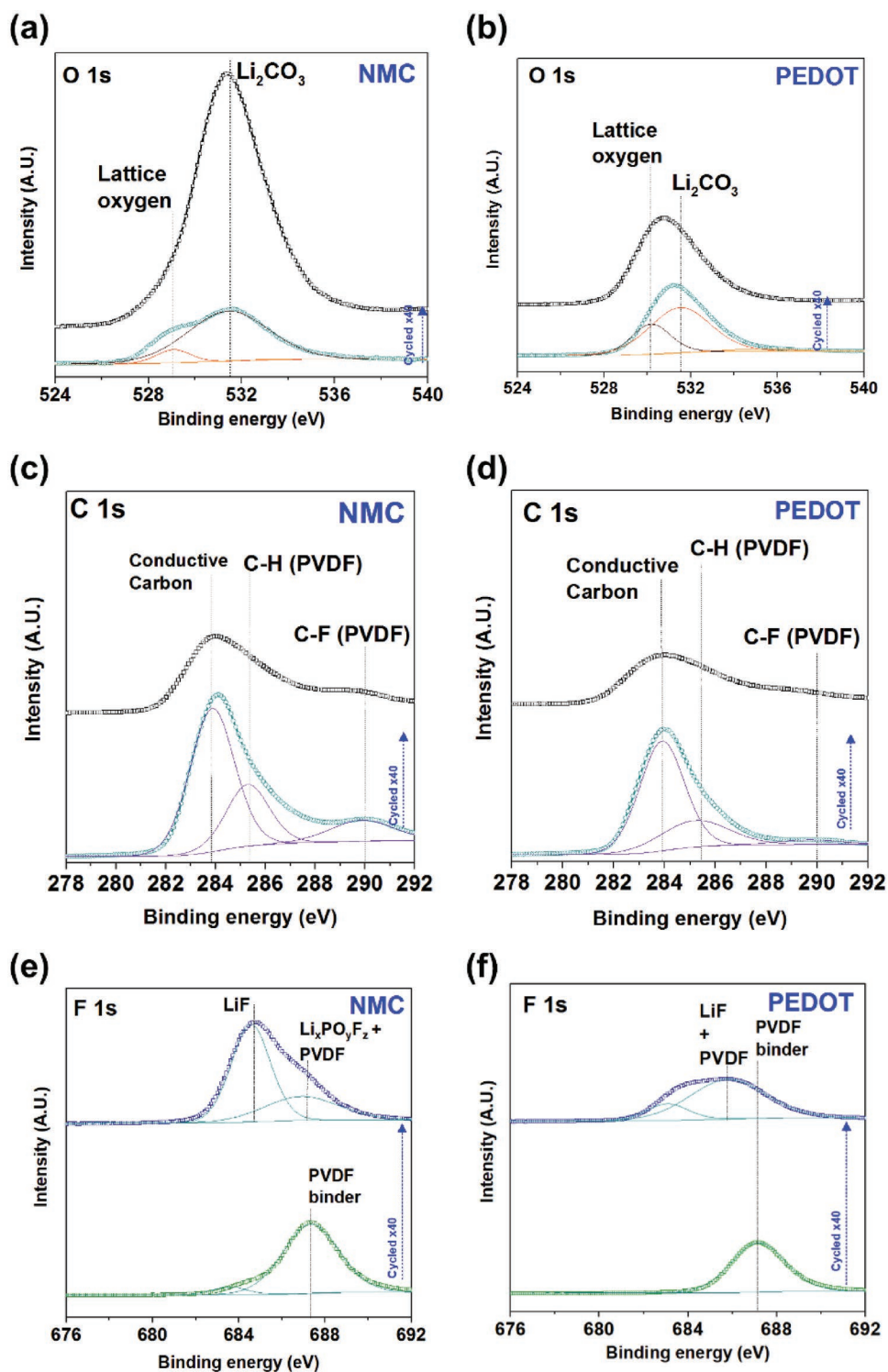
1801785 (6 of 13)

ADVANCED
SCIENCE NEWS
www.advancedsciencenews.com

ADVANCED
MATERIALS
INTERFACES
www.advmatinterfaces.de

Figure 4. a,b) XPS spectra for O 1s of the cycled bare Li(Ni$_{1/3}$Mn$_{1/3}$Co$_{1/3}$)O$_2$ (labeled as NMC) and PEDOT:PSS coated Li(Ni$_{1/3}$Mn$_{1/3}$Co$_{1/3}$)O$_2$ cathode (labeled as PEDOT). c,d) C 1s of the cycled NMC cathode and PEDOT cathode. e,f) F 1s of the cycled NMC cathode and PEDOT cathode.

NMC and 685.7 eV for PEDOT) was identified on both cathodes as shown in Figure 4e,f. However, the cycled NMC cathode showed a steep increment in the intensity of the LiF peak with a notable decrease in the peak intensity relevant to the PVDF binder. Moreover, there may be a new compound formed

consisting of similar species as Li$_x$PO$_y$F$_z$ within the energy range of 684–687 eV (Figure 4e), which is likely to be stemmed from the dissolution of the PVDF binder (687.2 eV). As for the PEDOT cathode, a peak was observed at ≈683 eV after cycling. This may be a new compound but mostly accumulated onto the

original PVDF material (Figure 4f). The presence of the LiF peak can be generally explained by the salt decomposition ($LiPF_6 \rightarrow PF_5 + LiF$) in the electrolyte. On the other hand, the growth of Li_2CO_3 can also result in the formation of LiF by the HF attack reaction ($Li_2CO_3 + HF \rightarrow 2LiF + H_2O + CO_2$). LiF is known as a stable compound but nonflexible and poorly conductive for the lithium ions and the electrons.[68,69] It is therefore likely that the improved rate capability of PEDOT cell is mainly due to the suppression of Li_2CO_3 and LiF compounds. The XPS spectra of the S 2p region between the pristine PEDOT and the cycled PEDOT cathode are shown in **Figure 5**a,b. In addition, energy-dispersive X-ray spectroscopy (EDX) mapping on the cycled PEDOT cathode is presented in Figure 5c. No sodium polystyrene sulfonate and poly(3,4-ethylenedioxythiophene) were identified by XPS after the electrochemical cycles (Figure 5b), implying that the PEDOT:PSS would not be involved in the formation of SEI layer due to its stable chemical property. EDX mapping exhibits the homogenous coating of PEDOT:PSS onto the cathode material, even after the severe battery cycling. The elements were mapped based on the $k\alpha$ spectra of EDX. The sulfur element was equally distributed with the transition metal oxides.

Figure 6 compares the magnetic properties and the powder diffractions between the cathodes. These measurements are chosen to obtain a detailed understanding of the electrode bulk property. No saturations were recorded in the magnetization chart for all samples (Figure 6a). This gives the evidence of antiferromagnetic interactions. Whereas the magnetization in the cycled NMC cell was notably different from other three cathodes, the cycled PEDOT cell revealed a similar magnetization curve as the reference materials. It is thus likely that PEDOT:PSS plays an important role in preserving the initial local atomic environment of each transition metal during charge–discharge. Figure 6b presents the reciprocal magnetic susceptibility of the cell cathodes. The paramagnetic behavior was observed above 150 K, and thus this domain was fitted according to the Curie–Weiss law of $X_m = C/(T - \theta)$, where C is the Curie constant ($C = N\mu^2/3k_B$, N is Avogadro's number, μ is effective moment, k_B is Boltzmann constant, and θ is the Curie–Weiss temperature. The values of the fitted θ were calculated to be −79.57 and −56.00 K for the NMC cathode at pristine state and the NMC cathode after cycling, respectively. As for PEDOT cathode at pristine state, the Curie–Weiss temperature was −74.05 K. This value changed to −65.99 K after PEDOT cell cycling. These negative values further support the antiferromagnetic interactions in this battery system. It is the interaction of the Ni^{2+} in the lithium layer with Ni^{2+} in the transition-metal layer and/or the other Ni^{2+} in the lithium layer that causes the antiferromagnetic interaction.[26,70] The Curie–Weiss fitting data are summarized in Table S1 (Supporting Information). The reciprocal magnetic susceptibility also revealed the existence of low-spin Mn^{3+} and low-spin Ni^{3+} on both cathode samples at the pristine state. This result accords with the occurrence of the trivalent Mn and trivalent Ni from the XPS measurements (Figure 3a–d). Again, the appearance of the low-spin elements can be explained by the instant electron transfer between Ni^{2+} and Mn^{4+} ($Ni^{2+} + Mn^{4+} \leftrightarrow Ni^{3+} + Mn^{3+}$).[71–73] Interestingly, the presence of the low spin elements was relatively higher for the PEDOT cathode
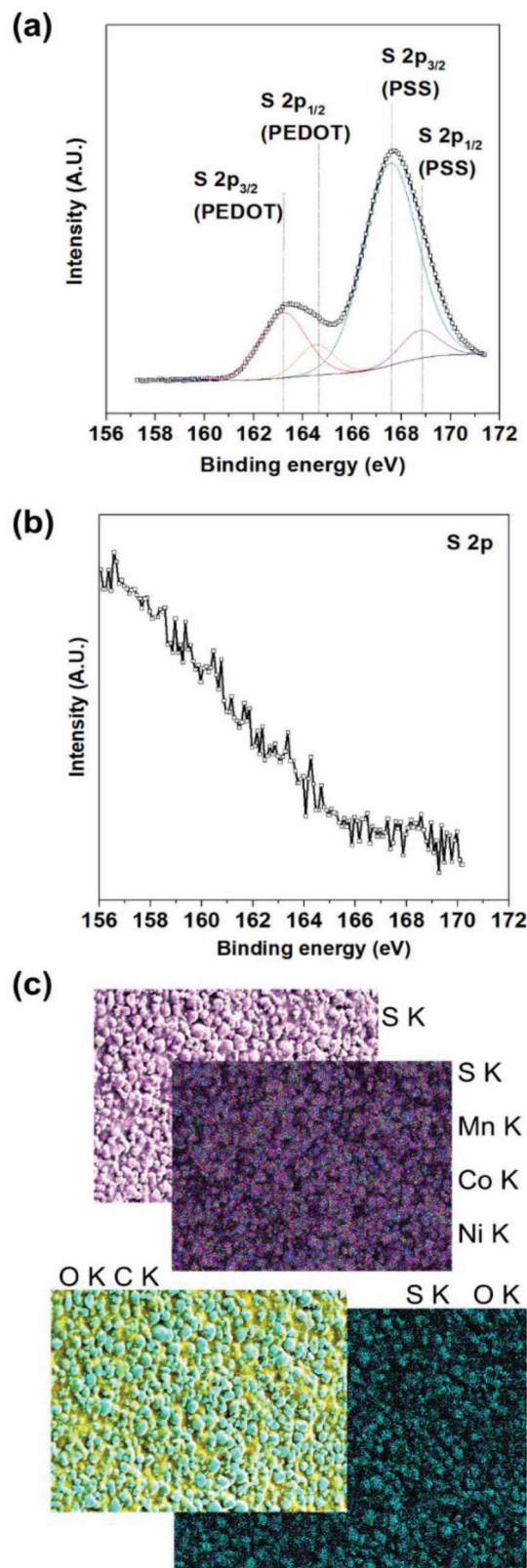

Figure 5. a,b) XPS spectra for S 2p of the cycled PEDOT:PSS coated $Li(Ni_{1/3}Mn_{1/3}Co_{1/3})O_2$ cathode (labeled as PEDOT) at pristine state and after cycling. c) EDX mapping of S K, Mn K, Co K, Ni K, O K, and C K of cycled PEDOT cathode.
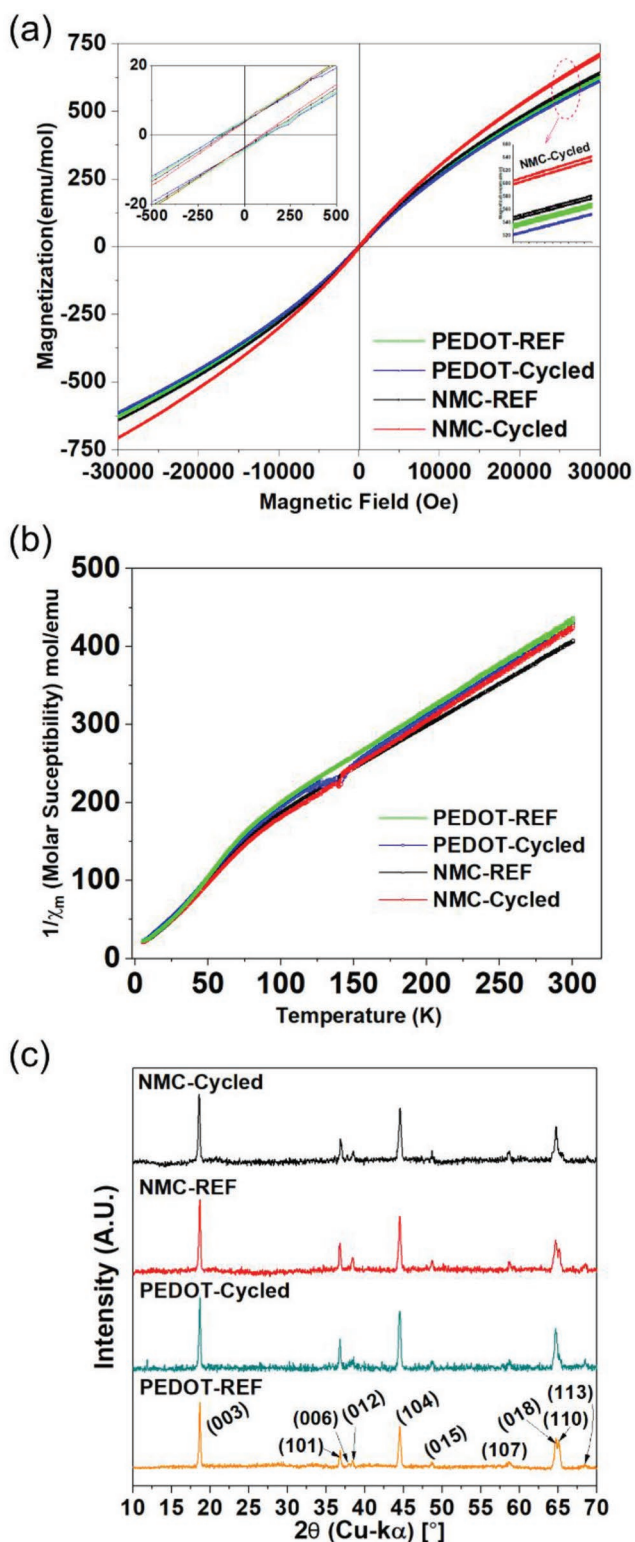
ADVANCED
SCIENCE NEWS
www.advancedsciencenews.com

ADVANCED
MATERIALS
INTERFACES
www.advmatinterfaces.de

Figure 6. a) Hysteresis loop of magnetization of the active material at 5 K of bare $Li(Ni_{1/3}Mn_{1/3}Co_{1/3})O_2$ at pristine state (NMC-REF), cycled $Li(Ni_{1/3}Mn_{1/3}Co_{1/3})O_2$ (NMC-cycled), PEDOT:PSS coated $Li(Ni_{1/3}Mn_{1/3}Co_{1/3})O_2$ at pristine state (PEDOT-REF), and PEDOT:PSS coated $Li(Ni_{1/3}Mn_{1/3}Co_{1/3})O_2$ after cycling (PEDOT-cycled). b) Reciprocal magnetic susceptibility between 5 and 300 K of the corresponding cathodes. The applied magnetic field is 1000 Oe. c) XRD measurements of the corresponded cathodes.

at the pristine state (refer Table S2, Supporting Information). This finding provides some support for the improvement of the electron transportation due to the PEDOT:PSS layer. After cycling, the effective magnetic moment in the NMC cathode was lower than the PEDOT cathode (refer to Table S2, Supporting Information). This might be related to the dissolution of the Mn into the electrolyte with the formation of SEI layer at the NMC cathode. In particular, the inclusion of the organic products in the SEI layer tends to reduce the effective magnetic moment. The powder diffraction obtained from X-ray diffraction (XRD) measurements is presented in Figure 6c. The XRD peaks can be indexed by an α-NaFeO$_2$ structure with the space group of $R\bar{3}m$. No important change was observed after the surface modification on the $Li(Ni_{1/3}Mn_{1/3}Co_{1/3})O_2$ cathode by PEDOT:PSS coating, showing a well-defined crystal structure of the layered structure. The cation mixing between Ni^{2+} and Li$^+$ was also evaluated by the intensity ratio of I_{003}/I_{104} in order to further examine the impact of the PEDOT:PSS coating on the base material. The value of I_{003}/I_{104} was measured to be 1.26 at the pristine state of the NMC cathode. After PEDOT:PSS coating, this value rather increased to 1.46, suggesting smaller cation mixing at the Li-ion layer and thus better rate capability as compared with the NMC cell.[74,75] Phase quantification and Rietveld refinement were also carried out on the electrodes (see Figure S1 and Table S3, Supporting Information). Spinel phases (cubic, $Fd\bar{3}m$) were identified in the NMC cathodes. The phase transition from layered structure into cubic spinel is a well-known cell fading process. By contrast, no spinel phases have been detected in the PEDOT cathodes, even after cycling.

Figure 7a–d displays the SIMS PID measurements expanded to the atomic mass of 60.0 amu, where the key transition metals are located. The present approach using depth profiling for each positive ion including some isotopes allows us to precisely visualize the distribution of target elements in the SEI layer of the battery cathode. It thus provides better insight into the key process involved in the improvement of the cell stability and performance by the conducting polymer. As mentioned earlier, Li$^+$ showed a concentration gradient between the surface and the bulk of the SEI layer formed upon charge–discharge of the NMC cell (Figure 7b). By contrast, this was not observed in the cycled cathode with the PEDOT:PSS coating. The present finding raises some intriguing questions in regard to the nature of the SEI layer grown. It is likely that the Li$^+$ diffusion in the SEI layer of the NMC cathode is strongly impeded by the presence of instable SEI components, such as LiF, Li$_2$CO$_3$, alkyl carbonates ((ROCO$_2$Li)$_2$ or ROCO$_2$Li), NiO, CoO$_x$, MnO$_x$, and Li$_2$O.[18] On the other hand, as for the PEDOT cell, Li$^+$ appears to be reversibly deintercalated to the host electrode after the last discharge down to 2.0 V, suggesting the formation of a stable SEI layer owing to the PEDOT:PSS coating. Especially, the suppression of the Li$_2$CO$_3$ and the LiF compounds, as evidenced from the XPS measurements (Figure 4), is likely to be the major cause that maintains the ionic conductivity of the PEDOT cell. Interestingly, there was also a significant difference in the carbon band located at around 12.0 amu between the NMC and PEDOT cathodes. At the reference state (REF), the PEDOT cathode exhibited a clear and continuous band of carbon whereas the NMC cathode
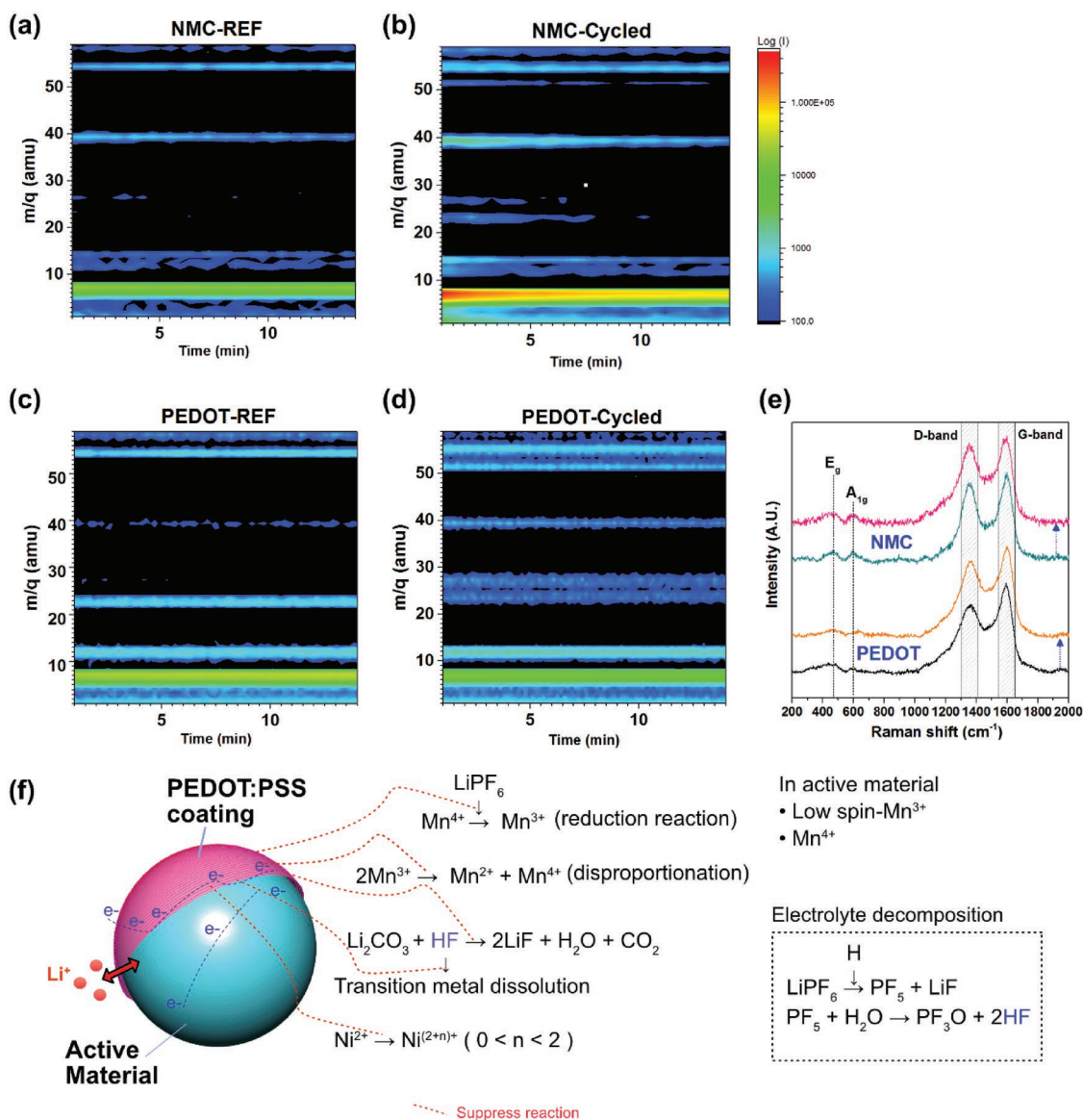
© 2019 The Authors. Published by WILEY-VCH Verlag GmbH & Co. KGaA, Weinheim

Figure 7. a,b) SIMS positive ion detection (PID) measurements on the surface interface of pristine $Li(Ni_{1/3}Mn_{1/3}Co_{1/3})O_2$ (labeled as NMC) and NMC cathode 40 times cycled in the voltage window of 2.0–4.2 V between C and 3C rate. c,d) PID of pristine $Li(Ni_{1/3}Mn_{1/3}Co_{1/3})O_2$ coated with PEDOT:PSS (labeled as PEDOT) and cycled PEDOT cathode with the same cycling condition as NMC. Y-axis represents the atomic mass of positive ions ($1 \leq m \leq 60$) including isotopes. Time is the sputtering time, which can be related to the depth of SEI layer. e) Raman spectra of the corresponding electrodes. Blue arrow indicates the cycling process starting from the reference state. f) A schematic illustration of the role of PEDOT:PSS coating in suppressing undesired side reactions and preserving transition metals from dissolution.

revealed an ambiguous and discrete carbon band with depth. The clarity of this carbon band has been increased on both cathodes after cycling (Figure 7b,d), yet the NMC cathode showed a blurry and wider carbon band with some defects. The occurrence of the intermittent defects in the NMC cathode could be explained by some oxidized carbons at the pristine state and the formation of the carbonate components after electrochemical cycles. The wider the band is, the more carbonates derivatives would be. It is therefore PEDOT:PSS that effectively maintains the surface chemistry of the active material as the coated electrode showed a consistent carbon band with a narrower range of the atomic mass around 12.0 amu. This result

can also be a case of the improvement in the mixing condition between the active material, carbon black, and PVDF binder in the electrode slurry by the conducting polymer. To obtain further information about the carbon states, Raman spectroscopy measurements were conducted. The Raman D-band and G-band were identified at ≈1352 and 1591 cm^{-1}, respectively, as shown in Figure 7e. Attention has been devoted to the peak intensity ratio of I_D/I_G, which can be used to assess some structural disorders in the graphitic material. The G-band is associated with the plane stretching motion of sp^2 carbon, while the D-band is related to the sp^2 defects and edge effects between carbons.[76–78] Hence, a higher ratio of I_D/I_G indicates larger

**ADVANCED
SCIENCE NEWS**

www.advancedsciencenews.com

**ADVANCED
MATERIALS
INTERFACES**

www.advmatinterfaces.de

defects in the graphitic system. The graphitic environment in the present electrodes comprises carbon black (Super C65) as a conductive additive. At pristine state, the I_D/I_G was measured to be 0.88 for the NMC cathode and 0.77 for the PEDOT cathode. The sp^2 carbon network of PEDOT cathode is more likely prominent than that of the NMC cathode. After cycling, the I_D/I_G ratio was 0.95 and 0.84 for the NMC and PEDOT cathode, respectively. It should be noted that the defects in the carbon environment of the cycled PEDOT cathode were even smaller than that of the uncycled NMC cathode. The Raman fingerprints for the layered structure of the lithium transition metal oxide were also identified at ≈475 cm^{-1} (E_g mode) and 600 cm^{-1} (A_{1g} mode). Similarly, as carbon, the transition metals (Mn, Ni, and Co) at the pristine state (REF) are equally distributed with depth in the PEDOT cathode, as evidenced by the SIMS PID measurements (Figure 7c). The major element that composes the band near 55.0 amu is Mn. The presence of Ni and Co corresponds to the band located at ≈59.0 amu. After cycling, some new bands appeared (≈51.0–52.0, ≈27.0, and ≈23.0 amu). The band at ≈51.0–52.0 amu could be attributed to the decomposed products (e.g., OF_2) from the electrolyte. The band at ≈27.0 amu could be ascribed to the formation of LiF, which can be originated from the salt decomposition reaction (LiPF$_6$ → PF$_5$ + LiF) and/or the decomposition of Li$_2$CO$_3$ by HF attack. On the other side, the band identified at ≈22.0–23.0 amu for PEDOT-REF must be interpreted with caution. More precisely, this band was located close to 22.0 amu whereas the band shown after cycling was close to 23.0 amu. The bright band observed at ≈22.0 amu is likely to be unique as it could be identified only for the PEDOT-REF samples (Figure 7c). The unique band can be ascribed to sodium from the sodium polystyrene sulfonate of PEDOT:PSS. Regardless of the element type, the PEDOT:PSS coated cathode displayed a continuous and homogenously distributed band pattern with depth after cycling. In contrast, NMC showed a discrete and wider band pattern with disfigures, implying inconsistency and complexity in the SEI layer. On the other side, the bands close to 58.0–60.0 amu became noticeable after the electrochemical cycles (NMC-cycled). This observation could be explained by the surface reconstruction with NiO, MnO$_x$, and CoO$_x$ and/or the precipitation of the decomposed transition metals (e.g., NiF$_2$, NiF$_3$, MnF$_2$, and CoF$_3$) onto the electrode surface.[18,28,79] Taken together, the conducting polymer plays an important role not only in preserving the initial transition metal states (as summarized in Figure 7f) but also rendering the electrode interface to a stable SEI layer, thereby improving the electrochemical performance of the cells.

3. Conclusions

The surface-modified NMC cathode with the conducting polymer has demonstrated notable improvements in the electrochemical performance due to the facilitated electron transportation. The mechanism involved for the performance improvement can be proposed with multiple factors. The conducting polymer not only protects the transition metals, which are the major source for the charge compensations, from the HF attack or the undesired redox reactions with the electrolyte,

but also effectively suppresses the formation of LiF and Li$_2$CO$_3$ on charge–discharge, thereby offering better Li$^+$ diffusion pathway. This treatment also appears to be effective in maintaining the initial local atomic environment of the bulk electrode. It thus showed a lower voltage decay in the galvanostatic profile of PEDOT cell with smaller amount of spectral shift at the reduction potential in the dQ/dV plot, implying less phase transition. In addition, the cathode treated with the conducting polymer revealed a higher metallic property at both reference and cycled states with lower work function changes as compared to NMC cathode. This suggests a good consistency in the surface environment of PEDOT cathode after the electrochemical cycles. An inherent problem of the layered oxide electrode is the crystal transformation from a layered structure into a spinel/rock salt structure that leads to a series of phase mismatches on charge–discharge, as we could see in the NMC cathode. This was also suppressed by the conducting polymer. We believe that the key process that leads to the notable improvement of the electrochemical performance and stability is the significant mitigation of the phase mismatches triggered by atomic state changes. The homogenous distributions of the interface components not only contribute to the increment of the charge capacity but also hinder the voltage decay on charge and discharge. The present study sheds some light on designing battery electrodes with enhanced stability and performance enabled by conducting polymers.

4. Experimental Section

Preparation of PEDOT:PSS Coating: The Li(Ni$_{1/3}$Mn$_{1/3}$Co$_{1/3}$)O$_2$/PEDOT:PSS composite was prepared by a wet coating method. 500 mg of Li(Ni$_{1/3}$Mn$_{1/3}$Co$_{1/3}$)O$_2$ active material (MTI, Japan) was dispersed in 10 mL PEDOT:PSS solution (Clevios PH1000), followed by adding 5 mL deionized water. The mixture was vigorously stirred for 12 h at room temperature. The solution was filtered and washed with alcohol and deionized water in order to collect the precipitate. Finally, the Li(Ni$_{1/3}$Mn$_{1/3}$Co$_{1/3}$)O$_2$/PEDOT:PSS was obtained after drying the precipitate at 60 °C for 12 h under vacuum.

Electrodes Preparation and Electrochemical Measurement: The Li(Ni$_{1/3}$Mn$_{1/3}$Co$_{1/3}$)O$_2$ (denoted as NMC) and the PEDOT:PSS coated (denoted as PEDOT) slurry was prepared by blending the Li(Ni$_{1/3}$Mn$_{1/3}$Co$_{1/3}$)O$_2$ (or @PEDOT:PSS) active material (MTI, Japan) with the PVDF binder and the carbon conductive additives (Super C65) in a weight ratio of 80:10:10 (= active material:carbon black:PVDF) in N-methyl-2-pyrrolidone (NMP, Sigma Aldrich) solution. The slurry was mixed for 24 h, and it was taken on the aluminum current collector for coating by an electrode coater equipped with a doctor blade and a dryer (MTI, Japan). The cast slurry was dried on the electrode coater at 60 °C for overnight. It was taken into the vacuum oven and dried at 120 °C for 12 h. Then, the cast film was roll-pressed to a thickness of 10 μm. The prepared electrodes were transferred into an Ar glove box to make CR2032 coin cells. The electrodes were cut into the discs with a diameter of 16 mm prior to assembling. The coin cell was assembled with Li metal as an anode, a polypropylene based membrane as a separator (CELGARD Inc.), a stainless steel spacer, and a steel spring using a hydraulic crimping machine (MTI, MSK-110) for sealing. The electrolyte was 1 M lithium hexafluorophosphate (LiPF$_6$) in ethylcarbonate (EC), diethylcarbonate (DC), and dimethylcarbonate (DMC) with the ratio of EC:DC:DMC = 1:1:1 in volume. The assembled coin cells were charged and discharged with the current rate of 1 C, 2 C, 3 C, and back to 1 C in the voltage window of 2.0–4.2 V at room temperature with 40 cycles for

**ADVANCED
SCIENCE NEWS**

www.advancedsciencenews.com

**ADVANCED
MATERIALS
INTERFACES**

www.advmatinterfaces.de

each cell. EIS was conducted using a Autolab PGSTAT204 with FRA32 module. EIS spectra obtained at the pristine state (REF) and the cycled state in the frequency range of 0.1 Hz to 100 kHz with an AC amplitude of 5 mV.

Electrode Material Characterization: The cycled coin cells were disassembled inside an Ar glovebox (H_2O level < 1 ppm and O_2 level < 1 ppm) and cleaned by DMC for the material characterization. They were dried overnight under the vacuum condition. Magnetic measurements were performed on the $Li(Ni_{1/3}Mn_{1/3}Co_{1/3})O_2$ (denoted as NMC-cycled) and the PEDOT:PSS coated $Li(Ni_{1/3}Mn_{1/3}Co_{1/3})O_2$ cathodes (denoted as PEDOT-cycled) by a physical property measurement system (Quantum Design PPMS Dynacool). The magnetic susceptibility of the electrodes was investigated under the magnetic field of 30k Oe at 5 K. Also, the molar magnetization was examined with 1000 Oe magnetic field in the temperature range of 5–300 K. A scanning electron microscope (SEM, FEI Quanta 250 FEG) was used to compare the morphology of the cathodes at different cycle states. The elemental mapping of S K, Mn K, Co K, Ni K, O K, and C K was conducted by EDX coupled with SEM. A Bruker D8 X-ray diffractometer (X-ray source: Cu Kα radiation) was utilized to measure the powder diffraction pattern. XRD spectra were collected by a scanning step of $0.02°$ in the range of $2\theta = 10°–80°$. Rietveld refinement and phase quantification were conducted with MAUD application. Raman peaks were obtained by a 3D laser Raman micro-spectrometer (Nanofinder 30, Tokyo Instruments) at five different points on each sample using a 532 nm excitation laser (green laser, spot size ≈ 2 μm) with 50x objective lens (Nikon) and 600 grooves mm^{-1} grating. The ex situ SEI study of the cathodes was conducted by an XPS (AXIS Ultra HSA KRATOS) using Al Kα (1486.6 eV) as the X-ray source. The operation condition was set to 15 kV and 150 W under ultrahigh vacuum (10^{-9} torr). A Shirley-type function was chosen to define the background of the spectra. The measured spectra were fitted based on a Gaussian–Lorentzian function using CasaXPS software. The collected spectra were calibrated by using C 1s as a reference. SIMS (Kratos Axis ULTRA) equipped with a quadrupole mass spectrometer (HAL 7, Hiden Analytical) and an ion sputter gun (IG20, Hiden Analytical) was utilized to collect the elemental signals in the PID mode. For sputtering and analysis in SIMS, 1 keV Ar+ primary beam with a 50 nA current and diameter of 100 μm was employed. The beam was at an angle of 45° with respect to the sample surface normal. The initial chamber pressure was 10^{-9} mbar, and the SIMS measurement was operated at a pressure of 10^{-6} mbar. With the ultrahigh vacuum environment, UPS measurements were also carried out. UPS calibration of the binding energy (eV) was performed by measuring the Fermi edge (E_F = 0 eV) on an Au surface. The applied bias voltage of the sample was −9 V, and the energy resolution is estimated to be 0.14 eV. During UPS operation, the photons were emitted by a helium gas (He I:21.22 eV) source.

Supporting Information

Supporting Information is available from the Wiley Online Library or from the author.

Conflict of Interest

The authors declare no conflict of interest.

[1] J.-M. Tarascon, M. Armand, *Nature* **2001**, *414*, 359.
[2] M. Armand, J. M. Tarascon, *Nature* **2008**, *451*, 652.
[3] R. Malik, F. Zhou, G. Ceder, *Nat. Mater.* **2011**, *10*, 587.
[4] K. Mizushima, P. C. C. Jones, P. J. J. Wiseman, J. B. B. Goodenough, *Mater. Res. Bull.* **1980**, *15*, 783.
[5] B. Dunn, H. Kamath, J. M. Tarascon, *Science* **2011**, *334*, 928.
[6] J. B. Goodenough, Y. Kim, *Chem. Mater.* **2010**, *22*, 587.
[7] K. Kang, Y. S. Meng, J. Bréger, C. P. Grey, G. Ceder, *Science* **2006**, *311*, 977.
[8] B. Scrosati, J. Garche, *J. Power Sources* **2010**, *195*, 2419.
[9] B. V. Ratnakumar, M. C. Smart, A. Kindler, H. Frank, R. Ewell, S. Surampudi, *J. Power Sources* **2003**, *119*, 906.
[10] J. R. Croy, A. Abouimrane, Z. Zhang, *MRS Bull.* **2014**, *39*, 407.
[11] M. M. Thackeray, S.-H. Kang, C. S. Johnson, J. T. Vaughey, R. Benedek, S. A. Hackney, *J. Mater. Chem.* **2007**, *17*, 3112.
[12] C. S. Johnson, N. Li, C. Lefief, J. T. Vaughey, M. M. Thackeray, *Chem. Mater.* **2008**, *20*, 6095.
[13] W. Liu, P. Oh, X. Liu, M.-J. Lee, W. Cho, S. Chae, Y. Kim, J. Cho, *Angew. Chem., Int. Ed.* **2015**, *54*, 4440.
[14] A. Manthiram, J. C. Knight, S. T. Myung, S. M. Oh, Y. K. Sun, *Adv. Energy Mater.* **2016**, *6*, 1501010.
[15] N. Nitta, F. Wu, J. T. Lee, G. Yushin, *Mater. Today* **2015**, *18*, 252.
[16] R. V. Chebiam, F. Prado, A. Manthiram, *J. Solid State Chem.* **2002**, *163*, 5.
[17] C. M. Julien, A. Mauger, K. Zaghib, H. Groult, *Inorganics* **2014**, *2*, 132.
[18] G. Cherkashinin, M. Motzko, N. Schulz, T. Späth, W. Jaegermann, *Chem. Mater.* **2015**, *27*, 2875.
[19] K. Hoang, M. Johannes, *Chem. Mater.* **2016**, *28*, 1325.
[20] M. Oishi, T. Fujimoto, Y. Takanashi, Y. Orikasa, T. Ina, H. Yamashige, D. Takamatsu, K. Sato, H. Murayama, H. Tanida, H. Arai, H. Ishii, C. Yogi, I. Watanabe, T. Ohta, A. Mineshige, Y. Uchimoto, Z. Ogumi, *J. Power Sources* **2013**, *222*, 45.
[21] L. Ni, O. Mn, S. Hy, W. Su, J. Chen, B. Hwang, *J. Phys. Chem. C* **2012**, *6*.
[22] C. F. Petersburg, Z. Li, N. A. Chernova, M. S. Whittingham, F. M. Alamgir, *J. Mater. Chem.* **2012**, *22*, 19993.
[23] X. Yu, Y. Lyu, L. Gu, H. Wu, S.-M. Bak, Y. Zhou, K. Amine, S. N. Ehrlich, H. Li, K.-W. Nam, X.-Q. Yang, *Adv. Energy Mater.* **2014**, *4*, 1300950.
[24] R. Hausbrand, G. Cherkashinin, H. Ehrenberg, M. Gröting, K. Albe, C. Hess, W. Jaegermann, *Mater. Sci. Eng., B* **2015**, *192*, 3.
[25] D. Mohanty, S. Kalnaus, R. A. Meisner, K. J. Rhodes, J. Li, E. A. Payzant, D. L. Wood, C. Daniel, *J. Power Sources* **2013**, *229*, 239.
[26] D. Mohanty, A. S. Sefat, S. Kalnaus, J. Li, R. A. Meisner, E. A. Payzant, D. P. Abraham, D. L. Wood, C. Daniel, *J. Mater. Chem. A* **2013**, *1*, 6249.
[27] M. Gu, I. Belharouak, J. Zheng, H. Wu, J. Xiao, A. Genc, K. Amine, S. Thevuthasan, D. R. Baer, J. G. Zhang, N. D. Browning, J. Liu, C. Wang, *ACS Nano* **2013**, *7*, 760.
[28] S.-K. Jung, H. Gwon, J. Hong, K.-Y. Park, D.-H. Seo, H. Kim, J. Hyun, W. Yang, K. Kang, *Adv. Energy Mater.* **2014**, *4*, 1300787.
[29] P. Yan, A. Nie, J. Zheng, Y. Zhou, D. Lu, X. Zhang, R. Xu, I. Belharouak, X. Zu, J. Xiao, K. Amine, J. Liu, F. Gao, R. Shahbazian-Yassar, J.-G. Zhang, C.-M. Wang, *Nano Lett.* **2015**, *15*, 514.

[30] F. Lin, D. Nordlund, Y. Li, M. K. Quan, L. Cheng, T.-C. Weng, Y. Liu, H. L. Xin, M. M. Doeff, *Nat. Energy* **2016**, *1*, 15004.

[31] S. Hwang, W. Chang, S. M. Kim, D. Su, D. H. Kim, J. Y. Lee, K. Y. Chung, E. A. Stach, *Chem. Mater.* **2014**, *26*, 1084.

[32] A. Jarry, S. Gottis, Y.-S. Yu, J. Roque-Rosell, C. Kim, J. Cabana, J. Kerr, R. Kostecki, *J. Am. Chem. Soc.* **2015**, *137*, 3533.

[33] A. M. Andersson, D. P. Abraham, R. Haasch, S. MacLaren, J. Liu, K. Amine, *J. Electrochem. Soc.* **2002**, *149*, A1358.

[34] J. Reed, G. Ceder, A. Van Der Ven, *Electrochem. Solid-State Lett.* **2001**, *4*, A78.

[35] T. Eriksson, A. M. Andersson, C. Gejke, T. Gustafsson, J. O. Thomas, *Langmuir* **2002**, *18*, 3609.

[36] K. Edstr, T. Gustafsson, J. O. Thomas, *Electrochim. Acta* **2004**, *50*, 397.

[37] T. Eriksson, A. M. Andersson, A. G. Bishop, C. Gejke, T. Gustafsson, J. O. Thomas, *J. Electrochem. Soc.* **2002**, *149*, A69.

[38] L. Guo, Y. Zhang, J. Wang, L. Ma, S. Ma, Y. Zhang, E. Wang, Y. Bi, D. Wang, W. C. McKee, Y. Xu, J. Chen, Q. Zhang, C. Nan, L. Gu, P. G. Bruce, Z. Peng, *Nat. Commun.* **2015**, *6*, 7898.

[39] Y. S. Lee, W. K. Shin, A. G. Kannan, S. M. Koo, D. W. Kim, *ACS Appl. Mater. Interfaces* **2015**, *7*, 13944.

[40] S. Kalluri, M. Yoon, M. Jo, S. Park, S. Myeong, J. Kim, S. X. Dou, Z. Guo, J. Cho, *Adv. Energy Mater.* **2017**, *7*, 1601507.

[41] J. B. Goodenough, K.-S. Park, *J. Am. Chem. Soc.* **2013**, *135*, 1167.

[42] T. M. Higgins, S. H. Park, P. J. King, C. Zhang, N. McEvoy, N. C. Berner, D. Daly, A. Shmeliov, U. Khan, G. Duesberg, V. Nicolosi, J. N. Coleman, *ACS Nano* **2016**, *10*, 3702.

[43] Y. Sun, S. Wang, H. Cheng, Y. Dai, J. Yu, J. Wu, *Electrochim. Acta* **2015**, *158*, 143.

[44] B. Zhang, R. Tan, L. Yang, J. Zheng, K. Zhang, S. Mo, Z. Lin, F. Pan, *Energy Storage Mater.* **2018**, *10*, 139.

[45] Y. Fu, A. Manthiram, *J. Phys. Chem. C* **2012**, *116*, 8910.

[46] D. H. Yoon, S. H. Yoon, K.-S. Ryu, Y. J. Park, *Sci. Rep.* **2016**, *6*, 19962.

[47] M. Yan, Y. Zhang, Y. Li, Y. Huo, Y. Yu, C. Wang, J. Jin, L. Chen, T. Hasan, B. Wang, B.-L. Su, *J. Mater. Chem. A* **2016**, *4*, 9403.

[48] J. Xu, J. Ma, Q. Fan, S. Guo, S. Dou, *Adv. Mater.* **2017**, *29*, 1606454.

[49] Z. Gong, Q. Wu, F. Wang, X. Li, X. Fan, H. Yang, Z. Luo, *RSC Adv.* **2015**, *5*, 96862.

[50] I.-H. Ko, S.-J. Kim, J. Lim, S.-H. Yu, J. Ahn, J.-K. Lee, Y.-E. Sung, *Electrochim. Acta* **2016**, *187*, 340.

[51] L. Groenendaal, F. Jonas, D. Freitag, H. Pielartzik, J. R. Reynolds, *Adv. Mater.* **2000**, *12*, 481.

[52] S. Niu, W. Lv, G. Zhou, H. Shi, X. Qin, C. Zheng, T. Zhou, C. Luo, Y. Deng, B. Li, F. Kang, Q. H. Yang, *Nano Energy* **2016**, *30*, 138.

[53] A. M. Nardes, M. Kemerink, M. M. de Kok, E. Vinken, K. Maturova, R. A. J. Janssen, *Org. Electron. Phys., Mater. Appl.* **2008**, *9*, 727.

[54] N. D. Trinh, M. Saulnier, D. Lepage, S. B. Schougaard, *J. Power Sources* **2013**, *221*, 284.

[55] X. Liu, H. Li, D. Li, M. Ishida, H. Zhou, *J. Power Sources* **2013**, *243*, 374.

[56] F. Wu, J. Liu, L. Li, X. Zhang, R. Luo, Y. Ye, R. Chen, *ACS Appl. Mater. Interfaces* **2016**, *8*, 23095.

[57] H. Li, M. Sun, T. Zhang, Y. Fang, G. Wang, *J. Mater. Chem. A* **2014**, *2*, 18345.

[58] N. Tran, L. Croguennec, C. Labrugère, C. Jordy, P. Biensan, C. Delmas, *J. Electrochem. Soc.* **2006**, *153*, A261.

[59] J. C. Hunter, *J. Solid State Chem.* **1981**, *39*, 142.

[60] I. Buchberger, S. Seidlmayer, A. Pokharel, M. Piana, J. Hattendorff, P. Kudejova, R. Gilles, H. A. Gasteiger, *J. Electrochem. Soc.* **2015**, *162*, A2737.

[61] K. Edström, T. Gustafsson, J. O. Thomas, *Electrochim. Acta* **2004**, *50*, 397.

[62] N. Yabuuchi, K. Yoshii, S.-T. Myung, I. Nakai, S. Komaba, *J. Am. Chem. Soc.* **2011**, *133*, 4404.

[63] Y. Deng, S. Liu, X. Liang, *J. Solid State Electrochem.* **2013**, *17*, 1067.

[64] N. N. Sinha, N. Munichandraiah, *ACS Appl. Mater. Interfaces* **2009**, *1*, 1241.

[65] Q. Li, C. Wang, Q. Li, R. Che, *RSC Adv.* **2016**, *6*, 105252.

[66] M. Xu, L. Zhou, Y. Dong, Y. Chen, J. Demeaux, A. D. MacIntosh, A. Garsuch, B. L. Lucht, *Energy Environ. Sci.* **2016**, *9*, 1308.

[67] E. Markevich, G. Salitra, D. Aurbach, *Electrochem. Commun.* **2005**, *7*, 1298.

[68] K. Tasaki, A. Goldberg, J.-J. Lian, M. Walker, A. Timmons, S. J. Harris, *J. Electrochem. Soc.* **2009**, *156*, A1019.

[69] K. Kanamura, *J. Electrochem. Soc.* **1995**, *142*, 340.

[70] G. Dutta, A. Manthiram, J. B. Goodenough, J.-C. Grenier, *J. Solid State Chem.* **1992**, *96*, 123.

[71] R. Prasad, R. Benedek, A. Kropf, C. Johnson, A. Robertson, P. Bruce, M. Thackeray, *Phys. Rev. B* **2003**, *68*, 012101.

[72] Z. F. Huang, F. Du, C. Z. Wang, D. P. Wang, G. Chen, *Phys. Rev. B* **2007**, *75*, 054411.

[73] Z.-D. Huang, X.-M. Liu, S.-W. Oh, B. Zhang, P.-C. Ma, J.-K. Kim, *J. Mater. Chem.* **2011**, *21*, 10777.

[74] T. Ohzuku, *J. Electrochem. Soc.* **1993**, *140*, 1862.

[75] A. Rougier, P. Gravereau, C. Delmas, *J. Electrochem. Soc.* **1996**, *143*, 1168.

[76] A. C. Ferrari, J. Robertson, *Phys. Rev. B* **2000**, *61*, 14095.

[77] A. C. Ferrari, *Solid State Commun.* **2007**, *143*, 47.

[78] R. Baddour-Hadjean, J.-P. Pereira-Ramos, *Chem. Rev.* **2010**, *110*, 1278.

[79] W. Li, A. Dolocan, P. Oh, H. Celio, S. Park, J. Cho, A. Manthiram, *Nat. Commun.* **2017**, *8*, 14589.